Gravitational radiation from radial infall of a particle into a Schwarzschild black hole. A numerical study of the spectra, quasi-normal modes and power-law tails.

Ermis Mitsou*

Département de Physique Théorique, Université de Genève, CH-1211 Geneva, Switzerland

The computation of the gravitational radiation emitted by a particle falling into a Schwarzschild black hole is a classic problem studied already in the 1970s. Here we present a detailed numerical analysis of the radiated waveforms, spectra and energies, improving significantly on the numerical accuracy of existing results and extending them to higher multipoles, up to $l = 6$. This is done by integrating the Zerilli equation in the frequency domain using the Green's function method. The resulting wave exhibits a "ring-down" phase whose dominant contribution is a superposition of the quasi-normal modes of the black hole. The numerical accuracy allows us to recover the frequencies of these modes through a fit of that part of the wave. Comparing with direct computations of the quasi-normal modes we reach a $\sim 10^{-4}$ to $\sim 10^{-2}$ accuracy for the first two overtones of each multipole. Our numerical accuracy also allows us to display the power-law tail that the wave develops after the ring-down has been exponentially cut-off. The amplitude of this contribution is $\sim 10^2$ to $\sim 10^3$ times smaller than the typical scale of the wave.

I. INTRODUCTION

The computation of the gravitational radiation due to a point-like particle falling into a black hole (BH) is a classic problem in General Relativity that received much attention in the 1970s [1–4] (see also the textbook [5] for discussion and further references).

The problem is of theoretical interest because it describes an elementary BH perturbation which, although relatively simple, exhibits characteristic features of more general perturbation scenarios. It is also a simple prototype of the much more complicated problem of the coalescence of binary BH systems, which plays an important role in the search for gravitational waves (GWs) at interferometers such as LIGO and Virgo.

The general features of the radiated waveform is by now well understood [3, 4, 6]. The first part of the signal the observer receives is called the *precursor* and corresponds to the radiation emitted directly from the in-falling source to the observer. It is therefore insensitive to what happens near the BH and it was shown in [7] that it can be well described by a resummation of the Post-Newtonian expansion. Then comes the *ring-down* phase which is dominated by a superposition of the quasi-normal modes (QNMs) of the BH. These are characteristic information of the Schwarzschild metric and are therefore brought by waves that were reflected in the neighborhood of the maximum of the effective potential of the problem (the "barrier"), situated at ~ 1.5 Schwarzschild radii. The QNMs are a very interesting feature also because they provide a possible bridge between classical and quantum gravity [8–11]. Finally, the wave exhibits a power-law tail at large values of the retarded time, after the ring-down has been exponentially cut-off. This residual radiation corresponds to waves that were not initially heading towards the observer but ended

up reaching him by scattering off the background metric at large distance of the horizon, hence the delay and the decrease in amplitude.

In this paper, we focus on the case where the infall is radial and starts at infinity with no initial velocity. The radiated energy spectrum and waveform can be computed from a numerical integration of a single wave-equation, the Zerilli equation [2], and this was already done in the original works [3] and [4]. Apart from a study of the case where it is falling from finite distance [12], to our knowledge, there have been no further numerical studies since then. Computations for high values of the angular momentum and a thorough analysis of the energy spectrum seem absent in the present literature.

The first part of our work consists in computing the spectra and waveforms for the $l = 2$ to 6 multipoles and also analyzing the energy spectra. The low accuracy in the original works [3, 4] did not allow such computations. With the computer resources available today, the accuracy can be significantly improved and our computation's relative error on the spectra is of order 10^{-5}. This allows us to cover well the asymptotic parts and extract their behavior. The waveforms, which are obtained by Fourier transforming the spectra, reach $\sim 10^{-4}$ and $\sim 10^{-3}$ at worst. For $l \leq 4$, we are able to keep that precision on a relatively large interval of retarded time which includes the beginning of the power-law phase. Once the waveform is obtained, we extract the QNM values by fitting the ring-down phase and then compare the results with the values obtained through direct computations [13, 14]. This way we determine how "visible" the QNMs are.

The organization of the paper is as follows. In section II we recall the main formulas describing the production of gravitational radiation from a radially in-falling test mass. In section III we present and discuss our results. All the equations present in our work can be found in [2–4]. Finally, an account of computational details and error estimation is presented in the appendix.

* Ermis.Mitsou@unige.ch

II. THEORETICAL BACKGROUND

In what follows, m and M are the masses of the particle and BH, respectively. We use units $G = c = 1$ and the following definition of the Fourier transform

$$\Psi_l(r,\omega) \equiv \frac{1}{\sqrt{2\pi}} \int \psi_l(r,t)e^{i\omega t}dt\,. \qquad (1)$$

The clear distinction in mass scales between the BH and the particle allows the problem to be treated within BH perturbation theory to first order. Therefore, the particle is a test mass, i.e. moving along the geodesics of the unperturbed Schwarzschild space-time, and produces a perturbation $h_{\mu\nu}$ (of the Schwarzschild metric) which is a test tensor field (on the Schwarzschild geometry) since we only keep first order terms of it in the Einstein equations. In the classic papers [1, 2], the authors showed that the linearized Einstein equations can be reduced to two independent one-dimensional scalar wave-equations for each l multipole (in the tensor spherical harmonics decomposition), where l represents the *total* angular momentum number. The wave-equation's effective potential term has no m dependence since the background metric is spherically symmetric. In the case of the radial infall of a particle, nor does the source term because of cylindrical symmetry. Thus the $m \neq 0$ modes are not excited. At each l, these equations describe the dynamics of the two eigenstates of the parity operator, which don't mix because of the symmetry of the background metric under parity, and together fully determine the 2^l-pole of $h_{\mu\nu}$. In the case of the radial infall of a particle, only the so called *polar* modes[1] are excited and we are left with one equation, the Zerilli equation. Denoting its solution by ψ_l, the radial dependence of the 2^l-pole of $h_{\mu\nu}$ is $\sim (1/r)\psi_l(t-r)$ in the radiation zone. The Zerilli equation on the frequency domain is [2]

$$\partial_{r_*}^2 \Psi_l + (\omega^2 - V_l(r))\Psi_l = S_l(r,\omega) \qquad (2)$$

where as usual $r_* = r + 2M\ln(r/2M - 1)$, and the effective potential is

$$V_l(r) = \left(1 - \frac{2M}{r}\right)$$
$$\frac{2\lambda^2(\lambda+1) + 3\frac{2M}{r}\lambda^2 + \frac{9}{2}\left(\frac{2M}{r}\right)^2 \lambda + \frac{9}{4}\left(\frac{2M}{r}\right)^3}{(\lambda r + 3M)^2} \qquad (3)$$

with $\lambda = (l-1)(l+2)/2$. The source term is

$$S_l(r,\omega) = -\frac{4m}{\lambda r + 3M}\sqrt{l+1/2}\left(1 - \frac{2M}{r}\right)$$
$$\left[\sqrt{\frac{r}{2M}} - i\frac{2\lambda}{\omega(\lambda r + 3M)}\right]e^{i\omega T(r)}\,, \qquad (4)$$

---

[1] They are the ones picking $(-1)^l$ under parity, i.e. the "true" scalar, vector, etc, as opposed to the "pseudo" ones picking $(-1)^{l+1}$, called *axial* modes.

where $T(r)$ is determined by the geodesic of the particle in the Schwarzschild metric,

$$\frac{T(r)}{2M} = -\frac{2}{3}\left(\frac{r}{2M}\right)^{3/2} - 2\left(\frac{r}{2M}\right)^{1/2}$$
$$+ \log\left[\left(\sqrt{r/2M} + 1\right)\left(\sqrt{r/2M} - 1\right)^{-1}\right]\,. \qquad (5)$$

The differential equation (2) is solved with boundary conditions of purely ingoing waves at the Schwarzschild radius and purely outgoing ones at infinity

$$\lim_{r_* \to -\infty} \Psi_l(r_*,\omega) = A_{l,in}(\omega)e^{-i\omega r_*}\,, \qquad (6)$$

$$\lim_{r_* \to \infty} \Psi_l(r_*,\omega) = A_{l,out}(\omega)e^{i\omega r_*}\,. \qquad (7)$$

These correspond to the fact that the source is always localized in space and therefore GWs can only be emitted *towards* the infinities. In order to compute the radiated amplitude of the ω-mode $A_{l,out}(\omega)$, it is convenient to use the Green's function method. Let $y_l^-(r_*,\omega)$ and $y_l^+(r_*,\omega)$ be the solutions of the homogeneous equation of (2)

$$\partial_{r_*}^2 y_l^{\pm} + (\omega^2 - V_l(r))y_l^{\pm} = 0 \qquad (8)$$

with boundary conditions

$$\lim_{r_* \to -\infty} y_l^-(r_*,\omega) = e^{-i\omega r_*}\,, \qquad (9)$$

$$\lim_{r_* \to \infty} y_l^+(r_*,\omega) = e^{i\omega r_*}\,, \qquad (10)$$

so that they match (6) and (7) in the final solution. At $r_* \to \infty$ the potential vanishes and y_l^- tends towards the analytical form.

$$\lim_{r_* \to \infty} y_l^-(r_*,\omega) = \alpha_l(\omega)e^{i\omega r_*} + \beta_l(\omega)e^{-i\omega r_*}\,. \qquad (11)$$

Thus the reflection and transmission coefficients of V_l for a monochromatic wave coming from plus infinity are

$$R_l = \left|\frac{\alpha_l(\omega)}{\beta_l(\omega)}\right|^2 \qquad T_l = \frac{1}{|\beta_l(\omega)|^2}\,, \qquad (12)$$

which we also compute for reasons made clear in section A 1. The Wronskian may be written $W_l(\omega) = 2i\omega\beta_l(\omega)$ and, in the radiation zone, one obtains

$$\Psi_{l,out}(r,\omega) = \lim_{r \to \infty} \Psi_l(r,\omega)$$
$$= \frac{e^{i\omega r_*}}{2i\omega\beta_l(\omega)} \int_{-\infty}^{\infty} S_l(\tilde{r}_*,\omega)y_l^-(\tilde{r}_*,\omega)d\tilde{r}_* \qquad (13)$$

which by definition of the outgoing ω-mode (7) gives

$$A_{l,out}(\omega) = \frac{1}{2i\omega\beta_l(\omega)} \int_{-\infty}^{\infty} S_l(\tilde{r}_*,\omega)y_l^-(\tilde{r}_*,\omega)d\tilde{r}_*\,. \qquad (14)$$

Given the choice of normalization in (1), the radiated energy spectrum of the l-mode is [2, 3]

$$\frac{dE_l}{d\omega} = \frac{1}{32\pi}\frac{(l+2)!}{(l-2)!}\omega^2|A_{l,out}(\omega)|^2\,. \qquad (15)$$

The waveform is found using the inverse Fourier transform. Introducing the retarded time $u \equiv t - r^*$, we have

$$\psi_{l,out}(u) = \frac{1}{\sqrt{2\pi}} \int_{-\infty}^{\infty} \Psi_{l,out}(r,\omega) e^{-i\omega t} d\omega$$

$$= \sqrt{\frac{2}{\pi}} \int_{0}^{\infty} \Re[A_{l,out}(\omega) e^{-i\omega u}] d\omega . \qquad (16)$$

The last equality comes from (7) and the fact that ψ_l is real, i.e. $A_{l,out}(-\omega) = \bar{A}_{l,out}(\omega)$. So the procedure consists in computing y_l^- through eq. (8) with initial condition given by eq. (9), and then evaluating (14) by extracting $\beta_l(\omega)$ out of eq. (11) and performing the integral. Once we have $A_{l,out}(\omega)$, the energy spectrum is given by (15) and the wave-function is computed through eq. (16).

III. RESULTS

In this section we present the results of our numerical integration. A detailed account of the numerical procedure and error estimation is given in appendices A and B, respectively. From now on we simplify the notation by dropping the "out" subscript in $A_{l,out}(\omega)$ and $\psi_{l,out}(\omega)$ and writing $f_l(\omega) \equiv dE_l/d\omega$. The figures are collected at the end of the paper.

A. Analysis of the frequency spectrum

The top and middle panels of figure 1 give the energy spectrum $f_l(\omega)$ in both linear and logarithmic scales, the modulus $|A_l(\omega)|$ and phase $\phi_l(\omega)$ (of $A_l(\omega)$). The shape of the energy spectra is in agreement with the result of ref. [3]. In table I we list the radiated energies for every 2^l-pole, that is

$$E_l = \int_0^\infty f_l(\omega) d\omega . \qquad (17)$$

To better characterize the energy spectrum, we have also computed the values $(\omega_l^\star, f_l^\star)$ at which $f_l(\omega)$ is maximal and the following quantities:

$$\langle\omega\rangle_l \equiv \frac{4M^2}{E_l} \int_0^\infty \omega f_l(\omega) d\omega , \qquad (18)$$

$$\sigma_l(\omega) \equiv \sqrt{\langle\omega^2\rangle_l - \langle\omega\rangle_l^2} . \qquad (19)$$

Summing over the angular momenta up to $l = 6$, we estimate the total radiated energy to be

$$\sum_{l=2}^{6} E_l = 0.010411(1) mc^2(m/M) , \qquad (20)$$

to be compared with the value $\simeq 0.0104 mc^2(m/M)$ given in [3]. To a first approximation, E_l seems to follow the

l	$M/(mc)^2 E_l$	$f_l^\star/m^2$	$2M\omega_l^\star$	$2M\langle\omega\rangle_l$	$2M\sigma_l(\omega)$
2	$9.1368(9)10^{-3}$	$3.5943(4)10^{-2}$	$0.61992(9)$	$0.5224(1)$	$0.1961(6)$
3	$1.1004(1)10^{-3}$	$3.3977(3)10^{-3}$	$1.0534(1)$	$0.8747(2)$	$0.271(1)$
4	$1.4947(1)10^{-4}$	$4.0757(4)10^{-4}$	$1.4685(2)$	$1.226(2)$	$0.329(2)$
5	$2.1380(2)10^{-5}$	$5.3971(5)10^{-5}$	$1.8688(2)$	$1.582(3)$	$0.375(3)$
6	$3.1423(3)10^{-6}$	$7.5273(8)10^{-6}$	$2.2726(2)$	$1.941(4)$	$0.413(4)$

TABLE I: From left to right: Multipole total radiated energy, energy spectrum's maximal value, corresponding frequency, mean value and standard deviation (for $f_l(\omega)$ seen as a distribution).

exponential trend proposed in [3], which is $\sim e^{-2l}$. We find that the form

$$E_l \simeq 0.56(3) l^{0.9(2)} e^{-1.75(5)l} mc^2(m/M) \qquad (21)$$

actually provides a better fit. Assuming that energies for $l > 6$ follow this empirical law, we get the order of the contribution of the neglected multipoles in (20) $E_{l>6} \sim 10^{-7} mc^2(m/M)$ which is less than our numerical precision.

We now turn ourselves to the asymptotic behavior of the spectra.

1. Low frequency limit

In this limit we find that our numerical results are very well fitted by

$$\log|\phi_l(\omega \ll 1) - \phi_l(\omega = 0)| \simeq a_l^\phi + b_l^\phi \log(\omega) \qquad (22)$$

and

$$\log(f_l(\omega \ll 1)) \simeq a_l^f + b_l^f \log(\omega) , \qquad (23)$$

that is, ϕ_l and f_l have a power-law behavior. Within our numerical precision, we find that, for the multipoles $l = 2, \ldots, 6$ that we have studied, $\phi_l(\omega = 0)$ is very well reproduced by[2]

$$\phi_l(\omega = 0) = \frac{\pi(l - 3)}{6} . \qquad (24)$$

In order to obtain the coefficients $a_l^\phi, b_l^\phi, a_l^f, b_l^f$ with great accuracy it is necessary to perform the fit in the very low frequency region. In Table II we show these coefficients, obtained by performing a fit at $2M\omega \sim 10^{-4}$, and we find that

$$f_l(\omega \ll 1) \sim \omega^{2l/3} \qquad (25)$$

reproduces our results very well.

_____

[2] Not directly computable because of the $1/\omega$ term in the source term, but through extrapolation.

l	a_l^ϕ	b_l^ϕ	a_l^f	b_l^f
2	1.38(1)	0.706(3)	$-1.84(6)$	1.321(8)
3	1.54(2)	0.707(2)	$-4.40(5)$	1.989(7)
4	1.64(1)	0.707(1)	$-6.92(4)$	2.653(6)

TABLE II: The first few fitting coefficients in eqs. (22) and (23).

l	a_l	b_l	c_l
2	5.34(2)	$-12.34(4)$	-3.03(8)
3	10.06(1)	$-12.26(3)$	-4.20(9)
4	14.81(1)	$-12.18(3)$	-5.42(3)
5	19.73(1)	$-12.17(4)$	-6.60(8)
6	24.81(2)	$-12.15(5)$	-7.7(2)

TABLE III: Fitting coefficients in eq. (30).

For $l = 2$ we are even able to go down to $2M\omega \sim 10^{-6}$ and we get

$$f_{l=2}(\omega \ll 1) \simeq 0.176(3)\,(2M\omega)^{1.332(2)} m^2\,. \qquad (26)$$

For each given l, the low frequency asymptotic behavior for $f_l(\omega)$ and $\phi_l(\omega = 0)$ can be computed analytically because it is due to the motion of the particle far from the horizon, where the trajectory can be well approximated by the Newtonian one and the GW emission can be computed using the multipole expansion in flat space. For $l = 2$ the contribution comes from the mass quadrupole and the computation is performed in ref. [15] (see also section 4.3.1 of ref. [5]). The result is

$$f_{l=2}(\omega \ll 1) = \left(\frac{2}{3}\right)^{7/3} \frac{\Gamma^2(1/3)}{5\pi}\,(2M\omega)^{4/3} m^2$$
$$\simeq 0.1774\,(2M\omega)^{4/3} m^2\,, \qquad (27)$$

so our numerical result (26) reproduces very well the exact analytic behavior. This is a significant check of our numerical procedure. We have also performed this analytical computation for $l = 3$ and again got agreement with eqs. (24) and (25). Both equations can be combined into

$$A_l(\omega \ll 1) \simeq a_l(i\omega)^{(l-3)/3}\,, \qquad (28)$$

where a_l is a positive real number. Finally, the $\phi_l(\omega)$ variation, which is not computable analytically, is found to be constant with respect to l within our error margins

$$\phi_l(\omega \ll 1) - \phi_l(\omega = 0) \sim \omega^{0.707}\,. \qquad (29)$$

2. High frequency limit

For this limit the full relativistic treatment is necessary and there is no simple analytical expression to compare with. Here we only focus on f_l. The top right panel of figure 1 clearly suggests an exponential cutoff. We find that the fitting form

$$\log f_l(\omega \gg 1) \simeq a_l + b_l\omega + c_l \log(\omega)\,, \qquad (30)$$

gives the best fit. Table III lists the resulting values for the parameters.

B. Waveforms and quasi-normal modes

In figures 2 to 6 we show, for $l = 2,\dots,6$, the amplitude spectrum $A_l(\omega)$, the waveform $\psi_l(u)$, the fit of

its ringdown phase using QNMs and its power-law tail (compared to the obtained QNM fit).

In the waveform plots, we observe that the number of significant oscillations in the ring-down increases with l while its typical length appears to be the same for all l. The precursor's typical length decreases with l. The typical amplitude decreases quite fast, as suggested by the empirical law in the corresponding energy (21).

As for the fit of the ring-down phase using QNMs, studies of more realistic scenarios such as the coalescence of a BH binary [16] have already shown very good results. It is therefore expected to work well in the case of the infalling particle model since it is numerically much simpler to treat. Table IV lists the results of the fit for the first three overtones while table V lists the values obtained through direct numerical computations, found in [13] for $l = 2$ and 3 and [14] for $l = 4, 5, 6$ (see appendix A, eq. (A3) for the fitting form). On the top panel of figure 7 we see that our error margins cover the expected values only for the first overtone ($n = 1$). Looking at the plots with the fitting curves, we see that the first mode's domination interval is pretty much the same for all l. On the other hand, the power-law contribution sets in later or is relatively weaker with increasing l. The high-l graphics are indeed the ones were the QNMs fitted the wave best, so the QNM contribution becomes more "visible" with increasing l. Inversely, in the case of $l = 2$, the power-law tail contribution sets in so early that it prevents us from even having a visible superposition of fit and data.

Finally, concerning the tail of the wave, analytical studies [6] show that it is actually a superposition of power-laws and that one has to go quite far in retarded time in order to see the leading term dominate. However, at such high values our precision breaks down so we cannot perform any useful fit but we still display the graphic result for $l = 2, 3, 4$ at lower u. The error on the $l = 5, 6$ cases is already notable at relatively low u.

computer resources.

l	$n=1$	$n=2$	$n=3$
2	$0.747(9) - i0.17(2)$	$0.45(3) - i0.51(9)$	
3	$1.198(2) - i0.18(1)$	$1.104(8) - i0.54(1)$	$0.93(4) - i1.5(3)$
4	$1.616(1) - i0.186(6)$	$1.580(8) - i0.552(6)$	$1.34(3) - i1.140(4)$
5	$2.025(1) - i0.190(4)$	$1.97(1) - i0.556(9)$	$1.82(4) - i0.895(8)$
6	$2.424(1) - i0.190(4)$	$2.378(8) - i0.572(9)$	$2.22(4) - i0.805(4)$

TABLE IV: Computed QNM values through waveform's fit.

l	$n=1$	$n=2$	$n=3$
2	$0.7473 - i0.1779$	$0.6934 - i0.5478$	
3	$1.1989 - i0.1854$	$1.1653 - i0.5626$	$1.1034 - i0.9582$
4	$1.6184 - i0.1883$	$1.5933 - i0.5687$	$1.5454 - i0.9598$
5	$2.0246 - i0.1897$	$2.0044 - i0.5716$	$1.9654 - i0.9607$
6	$2.4240 - i0.1905$	$2.4071 - i0.5733$	$2.3741 - i0.9611$

TABLE V: Direct computation QNM values.

[1] T. Regge and J. A. Wheeler, Phys. Rev. **108**, (1957), 1063.
[2] F. J. Zerilli, Phys. Rev. D **2**, (1970), 2141.
[3] M. Davis, R. Ruffini, W. H. Press and R. H. Price, Phys. Rev. Lett. **27**, (1971), 1466.
[4] M. Davis, R. Ruffini, J. Tiomno, Phys. Rev. D **5**, (1971), 2932.
[5] M. Maggiore, Gravitational Waves, Volume 1: Theory and Experiments, Oxford University Press, (2009).
[6] N. Andersson, Phys. Rev. D **55**, (1997), 468.
[7] T. Damour, Phys. Rev. D **79**, (2009), 064004.
[8] J. D. Bekenstein, Lett. Nuovo Cim. **11**, (1974), 467.
[9] S. Hod, Phys. Rev. Lett. **81**, (1998), 4293.
[10] E. Berti, gr-qc/0411025
[11] M. Maggiore, Phys. Rev. Lett. **100**, (2008), 141301.
[12] C. O. Lousto, R. H. Price, Phys. Rev. D **55**, (1996), 2124.
[13] E. W. Leaver, Proc. R. Soc. Lond. A **402**, (1985), 285.
[14] K. D. Kokkotas, private communication.
[15] R. V. Wagoner, Phys. Rev. D **19**, (1979), 2897.
[16] A. Buonanno, G. B. Cook and F. Pretorius, Phys. Rev. D **75**, (2007), 124018.

Appendix A: Computational details

In this section we present all the algorithms and techniques involved in the calculations. From now on we use only dimensionless variables. Thus, in what follows, ω, r_*, $A_{l,out}$, f_l, E_l and $\psi_{l,out}$ actually stand for $2M\omega$, $r_*/2M$, $A_{l,out}/(Mm)$, f_l/m^2, $M/m^2 E_l$ and $\psi_{l,out}/m$, respectively. Relative errors and margins are denoted using the symbol δ whereas Δ is used to denote absolute errors or integration grid steps, depending on the context.

1. The $\beta_l(\omega)$ parameter

Consider equation (11). The convergence towards that asymptotic form being too slow, we use the next order terms (as in [12]):

$$y_l^-(r_* \gg 1, \omega) \simeq \alpha_l(\omega)e^{i\omega r_*} + \beta_l(\omega)e^{-i\omega r_*} + \frac{1}{\omega r_*}\left(\gamma_l(\omega)e^{i\omega r_*} + \delta_l(\omega)e^{-i\omega r_*}\right) \quad \text{(A1)}$$

We take 47 equally spaced sample points over 5 typical periods[3] $2\pi/\omega$ on y_l^- and plug them in (A1). Having four complex unknowns, this gives us an overdetermined linear system $Ax = b$, where A is a 47×4 complex matrix and $x = (\alpha_l, \beta_l, \gamma_l, \delta_l)$. Then multiplying by A^T on the left we get a 4×4 matrix equation

$$A^T A x = A^T b, \quad \text{(A2)}$$

the solution of which minimizes the residue $||Ax - b||_2^2$. This equation is then solved using the Gaussian elimination method.

This routine is used repeatedly at increasing r_*, along with the computation of the integral in (14), thus making the result more and more precise[4]. Note that there is no direct check on the error of $\beta_l(\omega)$. However, the fluctuations of its value strongly affecting $A_l(\omega)$, we take the

————

[3] These values are chosen so as to increase the information input in our fit and also avoid repeating values which lead to a badly conditioned system.
[4] This is actually true only up to a certain limit because $A^T A$ contains three different orders of magnitude: (~ 1), $(\sim 1/r_*)$ and $(\sim 1/r_*^2)$, so if r_* is too large the problem is badly conditioned. In our case, however, we didn't reach that point.

latter's good convergence as a guarantee for an acceptable error on $\beta_l(\omega)$. A bit of monitoring at various stages of the computation confirms that the convergence of the $\beta_l(\omega)$ value is a lot faster than that of the integral in (14). Another source of confidence is the value $R_l(\omega) + T_l(\omega)$ (see eq. (12)) whose fluctuation around 1 also gives qualitative information on that error. In practice, we find a standard deviation of $\sim 10^{-6}$ on the ω-grid.

2. The radiation amplitude $A_l(\omega)$

For simplicity we write A for $A_l(\omega)$ since we describe the computation at a given value of ω and l. We use Numerov's method to integrate y_l^- in (8). Starting at finite $r_* \ll 0$, the initial condition corresponding to (9) is actually $e^{-i\omega r_*} \sum_{k>0} a_k(r-1)^k$ for some constants $a_k = O(1)$, at least for small k. We start at $r_* = -700$ because that's where $r - 1$ starts being computable ($\sim 10^{-300}$), in double precision. This allows us to neglect the correction to the initial condition (9). Since the source term is also negligible at $r_* = -O(100)$, the integral in (14), which is computed in the same loop as y_l^-, does not need any corrections for stating at finite r_* either. We use the trapezoidal rule for this integration because comparison with other Newton-Cotes formulae shows that it is the fastest method, in the sense that it starts approximating well at already big grid steps Δr_*. This is due to the oscillatory nature of the integrand making positive and negative errors approximately compensate each other. The overall convergence is dramatically slow because the source term (4) goes asymptotically as $\sim r^{-1/2}$. But the more we continue the more the integration's error grows. Therefore, we have to use a special method in order to extract that limit faster.

We define $A(r_*)$ as being the value of (14) where the integral is truncated on the upper bound at r_*, so that $A = \lim_{r_* \to \infty} A(r_*)$ (remember, the ω and l dependence is implicit here). On the actual r_{*k} grid (the discretized axis), the computed sequence $A(r_{*k})$ approximating that value gives a damped oscillation. We divide the r_*-axis into intervals of length L which is given by a few typical periods $2\pi/\omega$ and index them by $n = 0, 1, 2, \ldots$. We choose to consider only the average value of $A(r_{*k})$ out of every such interval, call it A_n (its phase ϕ_n), a new sequence sharing the same limit. So L is a smoothing parameter. We also calculate β_l (and α_l) at every n using the procedure described in section A 1. The routine stops when the last ten values of $|A_n|^2$ and ϕ_n are all within an $\epsilon = 10^{-4}$ margin around their respective mean values and gives the latter as a result for A. The ϵ margin is actually a relative one for $|A|^2$ whereas it is an absolute one for ϕ. Thus, if we let the greatest distances from the mean values be denoted by $\Delta(|A|^2)$ and $\Delta\phi$, the condition reads $\delta(|A|^2) \equiv \Delta(|A|^2)/|A|^2 < \epsilon$ and $\Delta\phi < \epsilon$.

Once that loop has finished, we start all over again but with half the previous Δr_* step. This goes on until the difference between two consecutive such computations is again less than ϵ (again, relative for $|A|^2$ and absolute for ϕ). When finished, we pass to the next ω value.

As for the ω-grid parameters, let $\Delta\omega_l$ be the step and $\omega_{l,max}$ be the maximum value for which we perform the previous computation. It appears that $\omega_{l,max} \sim (l + 1)$ is a good choice, as can be seen by looking at the $A_l(\omega)$ plots (top left panels of figures 2 to 6) where we have set $(l+1)/2$ for the maximum of the displayed ω axis. This is why we chose $\Delta\omega_l = 6(l+1)10^{-5}$, so that the precision is the same for all l. However, we did not choose the $\omega_{l,max}$ value to follow the $\sim (l + 1)$ trend. We find instead that there is a natural limit on the ω axis for the convergence of the $A_l(\omega)$ computation, given our precision criteria. After a given value for f_l, apparently common to all l the program keeps dividing the Δr_* step without ever meeting the required precision. Since the values at $\omega \gg 1$ are important for the computation of the tail of the waveform, we set the $\omega_{l,max}$ value the higher we can, that is to that natural limit. This also sets $l = 6$ as our limit for l, because the computation for $l = 7$ would not give enough points for the spectrum at large frequencies.

3. The radiated waveform $\psi_l(u)$ and energy spectrum integrals $E_l, \langle\omega\rangle_l$ and $\sigma_l(\omega)$

We consider equations (16), (17), (18) and (19). We use a high order Newton-Cotes formula for their integration, the one with 7 stages and of order 8, named Weddle's formula. We also use Richardson's extrapolation on the integrals computed with steps $\Delta\omega$ and $2\Delta\omega$ in order to further increase our precision.

For $\psi_l(u)$, the $l = 2$ case must be treated carefully because $A_{l=2}(\omega)$ diverges at the origin. It is true that, for any value of l, we can only compute $A_l(\omega)$ for $\omega > 0$ because of the ω^{-1} factor in the source term. However, we know from (28) that $A_{l=3}(\omega = 0)$ is finite and therefore deducible by extrapolation and $A_{l>3}(\omega = 0) = 0$. For $l = 2$, the $[0, \Delta\omega]$ contribution cannot be extrapolated. It can however be approximated through the integrand's analytic behavior at $\omega \to 0$ (discussed in section III A, neglecting the $\phi(\omega)$ variation). Plugging the later in $\int_0^{\Delta\omega} \Re[A_{l=2}(\omega)e^{-i\omega u}]d\omega$ we obtain a solution involving generalized hypergeometric functions and we Taylor expand them until the desired precision is reached.

4. Extraction of the QNMs out of the signal

We know that the QNMs are getting more damped with increasing n. Thus, if we look far enough in the ringdown phase of the wave, the least damped mode ($n = 1$) should dominate. However, the more we go at large u to look for the first mode the more the tail contribution becomes notable. So our fitting model is

$$B_{l,n}e^{\omega_{l,n,\Im}u}\sin(\omega_{l,n,\Re}u + \theta_{l,n}) + h_{l,n}, \qquad (A3)$$

where the last term is an offset which can help compensate the shift due to the slowly appearing tail. It is really necessary for low l but becomes negligible for high l. Once we have found the first overtone ($n = 1$), we subtract it from the waveform and reapply the fit seeking the second one ($n = 2$) and so on.

Since there is no prescription for finding the ideal interval on the u axis to perform the fit we run a small program which tries all possible intervals in $[0, 30]$, retaining every time the value of the resulting fitting parameters. This gives us a 3D plot for each one of them, where the floor axes are given by the values of the interval's boundaries. The plots for $\omega_\Re$ and $\omega_\Im$ exhibit some flat areas at equal height corresponding to the ensemble of intervals at which the fit was optimal. We then cut the plot in horizontal slices of a given thickness Δz and create a histogram giving the number of points which lie inside each one of those slices. The maximum of that histogram gives us the researched value with absolute error $\Delta z / 2$ but when the spike is not clear enough we take half its width for an estimation of the error instead. For $n > 1$ we sometimes obtain more than one maximum so we choose based on the coherence with the rest of the data and by looking at the 3D plot in order to identify "false" flat areas. The bottom of figure 7 gives an example of the 3D graphic and its histogram. As for the B and θ parameters in (A3), no such flat area is obtained after the first fit series so we run the program one more time but with the $\omega_\Re$ and $\omega_\Im$ values already inserted.

Appendix B: Error estimation

1. Radiated spectrum $A_l(\omega)$ and $f_l(\omega)$

Almost all the computed points meet the precision criteria of section A 2, meaning an estimated $\sim 10^{-5}$ precision on $|A_l|^2$ and ϕ and therefore on $|A_l|$ and f_l (remember that it is an absolute error for ϕ). The only exceptions are for $l \geq 4$ where points with ω close to zero ($\omega \sim 10^{-3}$) have an error of $\sim 10^{-3}$. However, $|A_l|$ is very small there and the absolute error it causes in the calculation of E_l and ψ_l is thus negligible. In order to decrease it as much as possible anyway, we have extrapolated those regions using the analytical low frequency behavior discussed in section III A.

As for the asymptotic behavior fits, in most cases such as in the high frequency region, there is no prescription for the ideal interval to fit on, so we estimate the error on the fitting parameters by their variation when fitting on different intervals. If, however, the number of points is small, leaving no choice about the fitting interval, the error corresponds to a 95% c.l.

2. Radiated energy spectrum characteristics (table I)

There are three types of error in the computation of the integrals E_l, $\langle \omega \rangle_l$ and $\sigma_l(\omega)$: the one due to the relative error on the integrand, noted δ_i, the one due to the discreteness of the integration domain, noted δ_d, and the one due to its finiteness, noted δ_f. δ_d is estimated by the relative difference of two integrations with grid steps $\Delta\omega$ and $2\Delta\omega$ and δ_f is estimated using (30). For E_l we have $\delta_i \sim 10^{-5}$ since $f_l(\omega) \sim |A_l(\omega)|^2$, $\delta_d \sim 10^{-7}$ and $\delta_f \sim 10^{-8}$ so $\delta(E_l) \sim 10^{-5}$. For $\langle \omega \rangle_l$ and $\sigma_l(\omega)$, we use

$$\Delta p(x_1, ..., x_n) \approx \sum_{k=1}^{n} \left| \frac{\partial p}{\partial x_k} \right| \Delta x_k \qquad \text{(B1)}$$

for the δ_i and find $\delta_i(\langle \omega \rangle_l) = 2.10^{-4}$ and $\delta_i(\sigma_l(\omega)) = 2.10^{-4}(1 + 2\frac{\langle \omega \rangle_l}{\sigma_l(\omega)})$. The δ_d and δ_f are again smaller. Finally, for the maximum $f_l^\star$ we record the smallest gap between its value and its direct neighbor's on the ω grid. However, this value is inside $f_l^\star(1 \pm \epsilon)$, so the relative error for $f_l^\star$ is also given by ϵ. For the error on $\omega_l^\star$ we simply take half the ω grid step.

3. Radiated waveform $\psi_l(u)$

First of all, being interested in the domain $u \in [-50, 200]$ for $l \leq 4$ and $[-50, 50]$ for $l = 5$ and 6, the greatest gap between two consecutive ωu values in the oscillatory term of (16) is $(u\Delta\omega)_{max} = 0.06 \ll \pi$. Thus the ω-grid is dense enough to take into account even the sharper variations of the integrand. The sources of error are the same as in the previous section although here we are going to use the absolute analogues for δ_f and δ_d. The relative ones vary a lot near the zeros of the waveform and aren't therefore very meaningful. Δ_f is estimated using (30) and (15) to obtain the behavior of $|A_l(\omega)|$

$$|A_l(\omega \gg 1)| \approx \sqrt{128\pi \frac{(l-2)!}{(l+2)!}} e^{(a_l + b_l \omega)/2} \omega^{c_l/2 - 1}. \quad \text{(B2)}$$

Then

$$\Delta_{f,l}(u) \approx \frac{1}{\sqrt{2\pi}} \int_{\omega_{l,max}}^{\infty} |A_l(\omega \gg 1)| \cos(u\omega) d\omega \quad \text{(B3)}$$

is a good estimation of the absolute error due to the neglected part of the frequency domain. Table VI shows the typical values for Δ_d and Δ_f which fluctuate well inside the given order. It also gives the maximum values of the corresponding waveforms in order to compare the scales.

The regions where the relative error is maximal are of course the ones near zeros and towards the end of the tail. In the latter case, we reach $\sim 10^{-3}$ at worst with one exception, the case of $l = 2$ where it goes till $\sim 10^{-2}$ at the same places. Otherwise, the majority of points has

l	Δ_d	Δ_f	$|\psi|_{l,\max}$
2	10^{-8}	10^{-5}	4.2×10^{-1}
3	10^{-8}	10^{-9}	3.8×10^{-2}
4	10^{-9}	10^{-8}	6.3×10^{-3}
5	10^{-9}	10^{-10}	1.2×10^{-3}
6	10^{-10}	10^{-11}	2.6×10^{-4}

TABLE VI: Typical values of Δ_d and Δ_f and reference scales

$\sim 10^{-4}$ or even 10^{-5}. Finally, the error due to the one of the integrand is $\delta_i \sim 10^{-5}$ (see section A 2).

As for the QNM, we have already explained how the errors are computed (see section A 4).
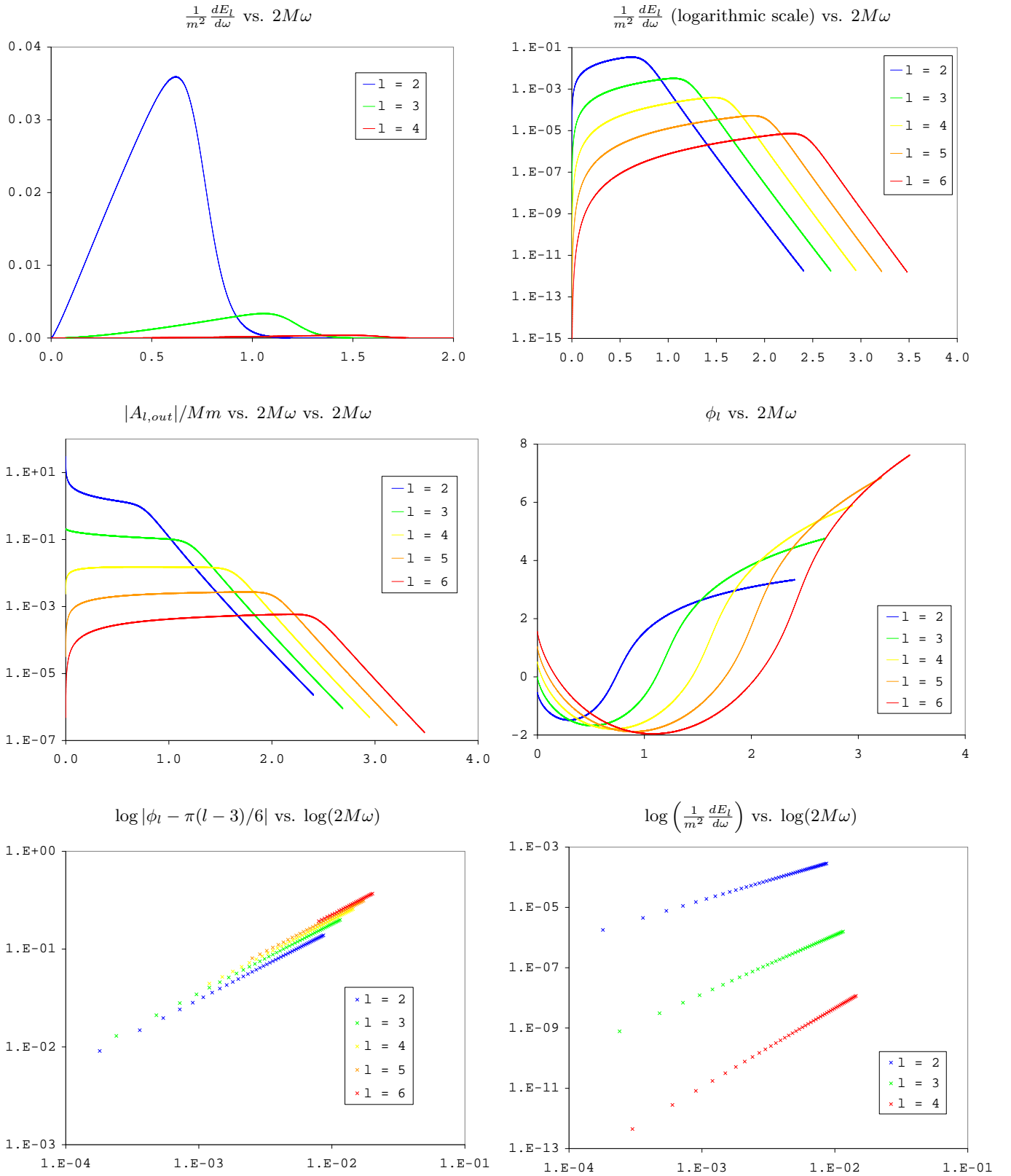
FIG. 1: Top panels: the energy spectra $1/m^2 dE_l/d\omega$ on normal and logarithmic scale. Middle panels: The amplitude spectra, modulus (logarithmic scale) and phase. Bottom panels: low frequency asymptotic behavior of the energy spectra and phases.
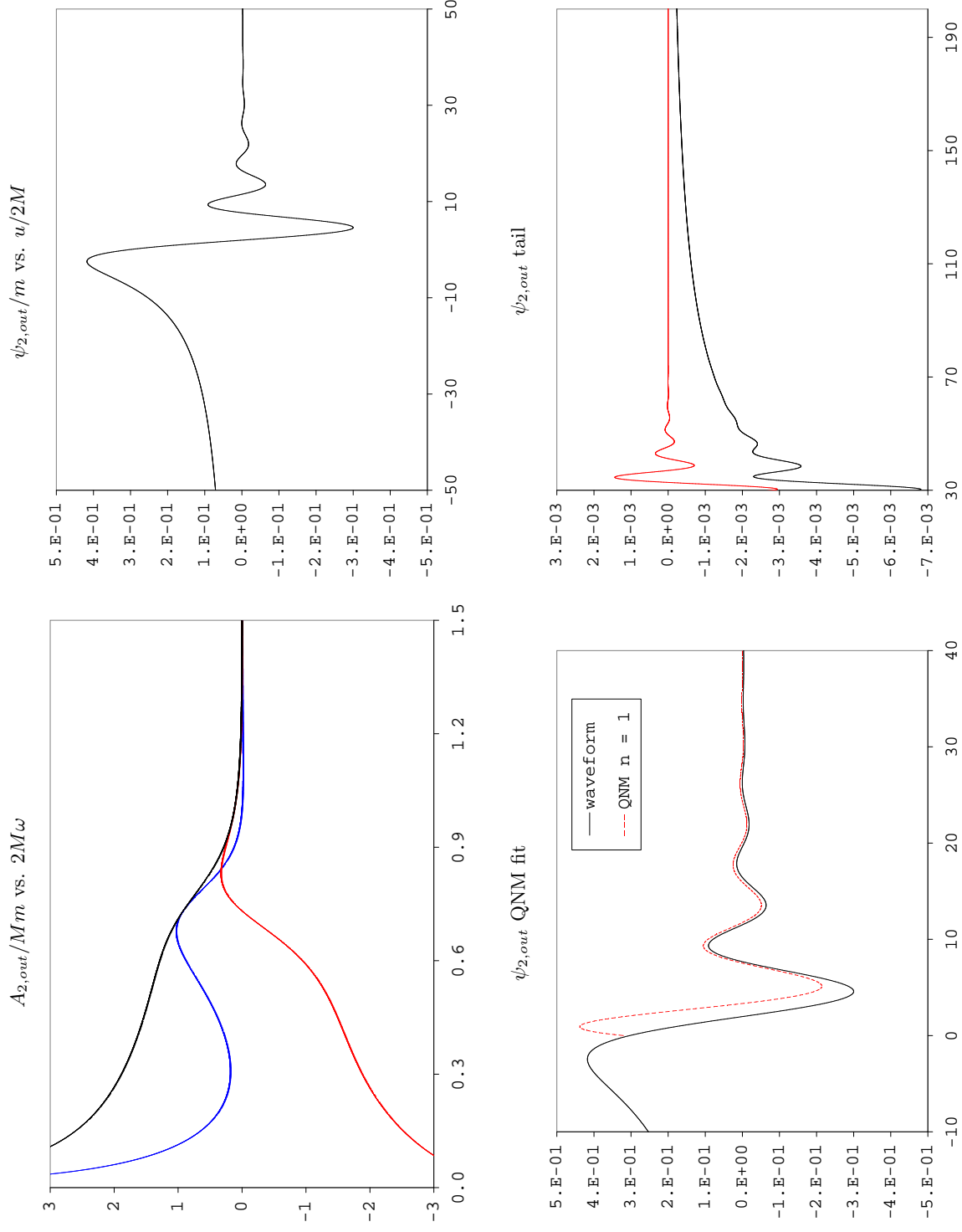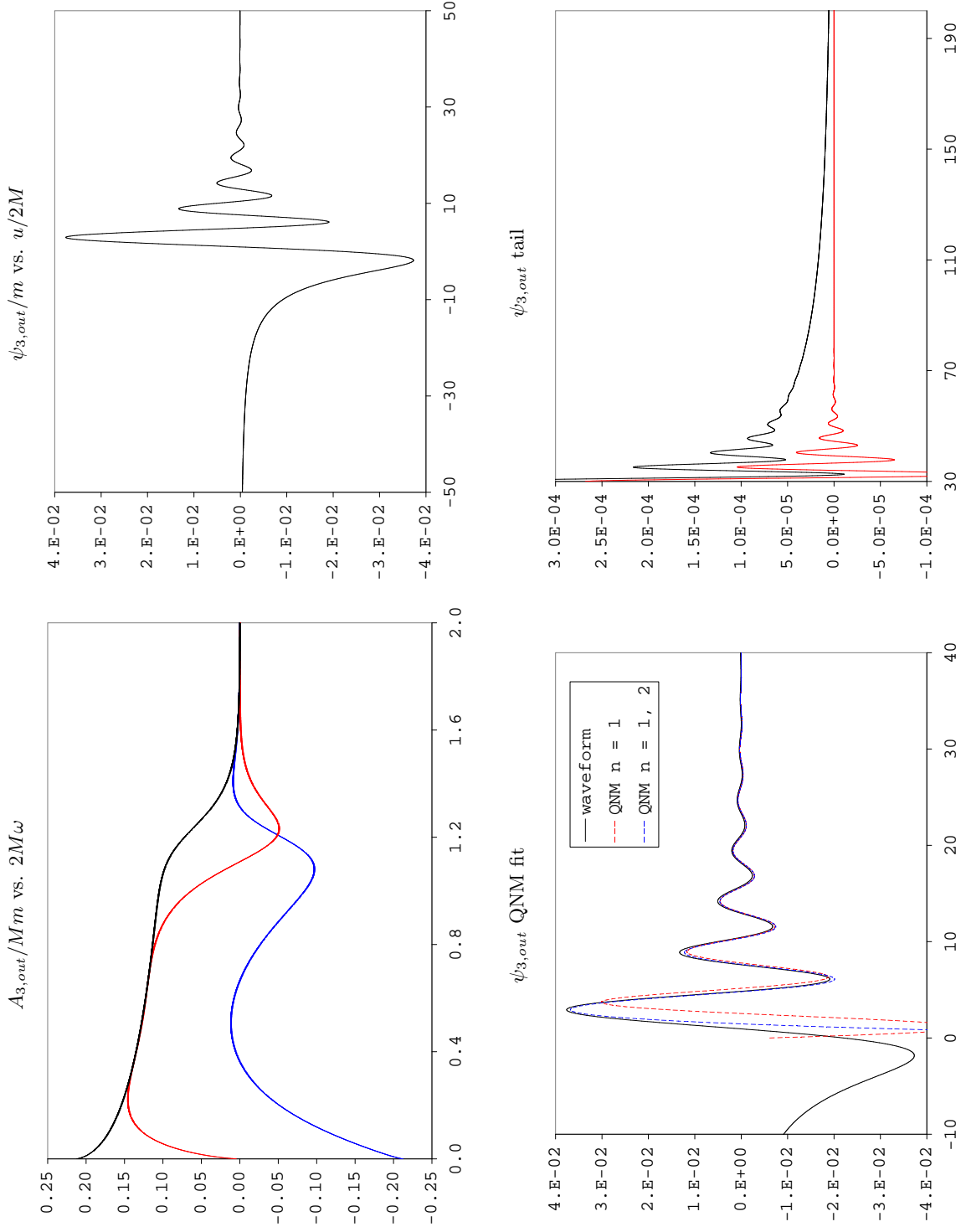
FIG. 2: Top left panel: the amplitude $A_{2,out}/Mm$. Top right panel: the waveform $\psi_{2,out}/m$. Bottom left panel: the curve corresponding to the first mode of the QNM contribution. Bottom right panel: the power-law tail of $\psi_{2,out}/m$ compared to the QNM contribution.

FIG. 3: Top left panel: the amplitude $A_{3,out}/Mm$. Top right panel: the waveform $\psi_{3,out}/m$. Bottom left panel: the curves corresponding to the QNM contribution up to the second overtone $n = 2$. Bottom right panel: the power-law tail of $\psi_{3,out}/m$ compared to the QNM contribution.
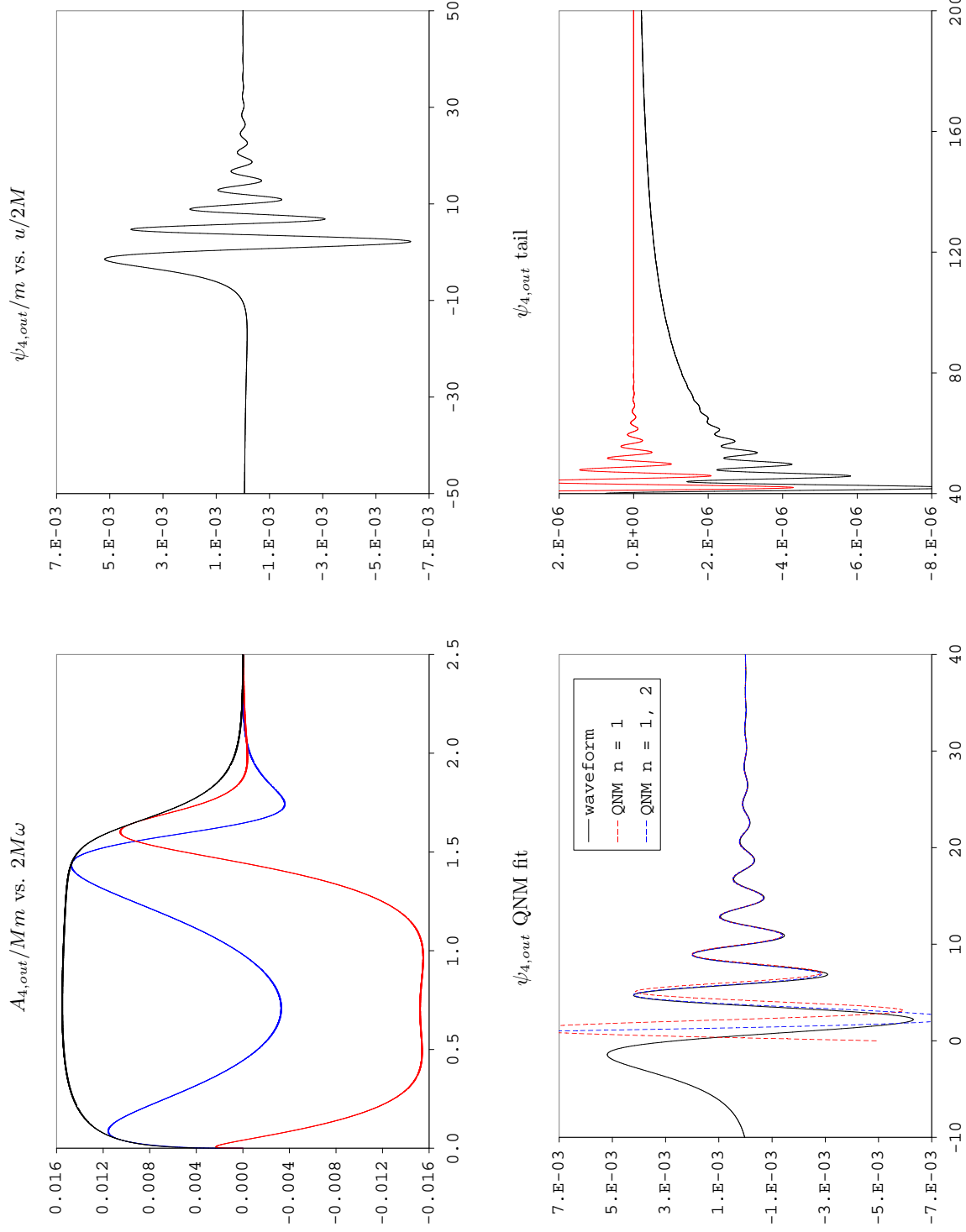
FIG. 4: Top left panel: the amplitude $A_{4,out}/Mm$. Top right panel: the waveform $\psi_{4,out}/m$. Bottom left panel: the curves corresponding to the QNM contribution up to the second overtone $n = 2$. Bottom right panel: the power-law tail of $\psi_{4,out}/m$ compared to the QNM contribution.
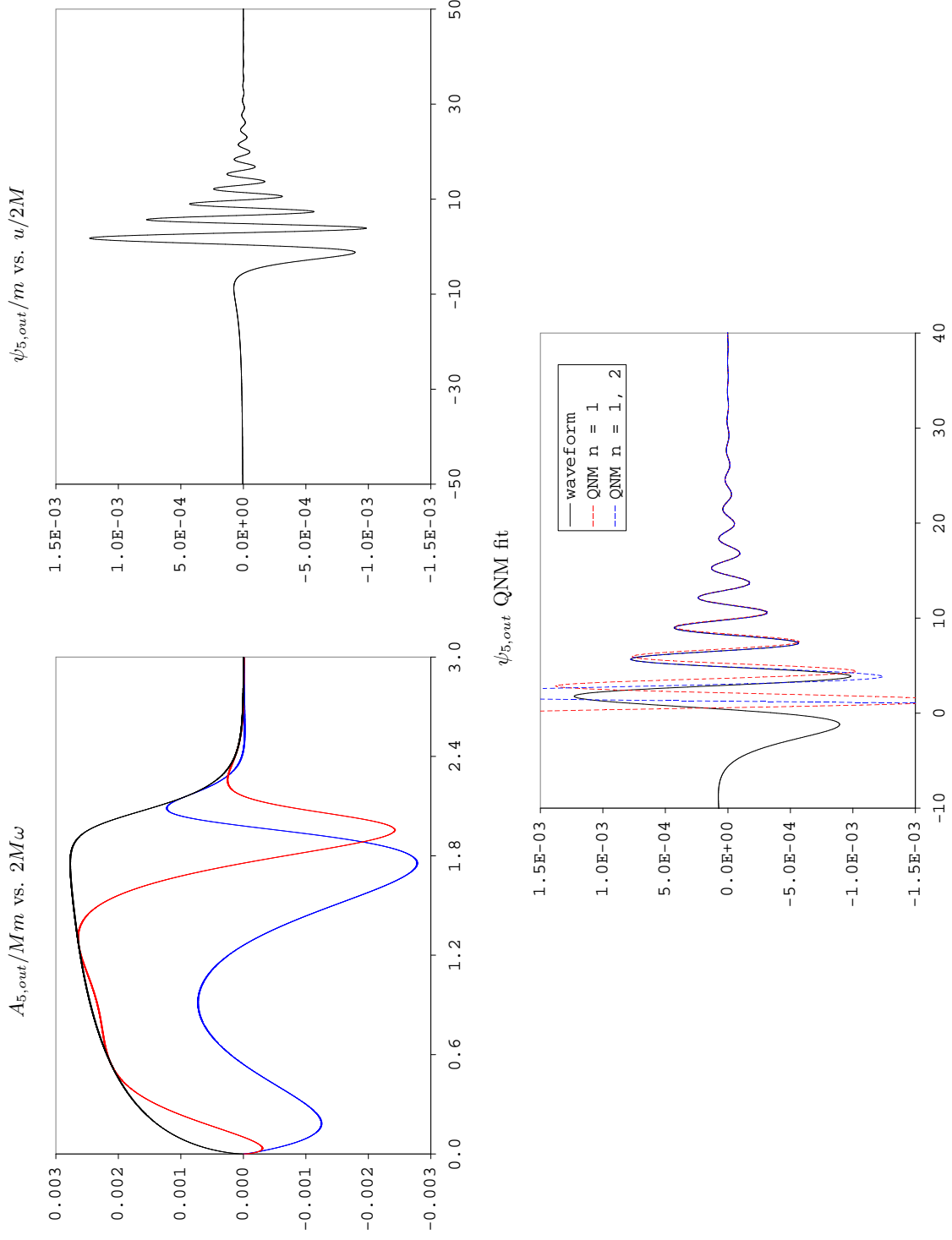
FIG. 5: Top left panel: the amplitude $A_{5,out}/Mm$. Top right panel: the waveform $\psi_{5,out}/m$. Bottom panel: the curves corresponding to the QNM contribution up to the second overtone $n = 2$.

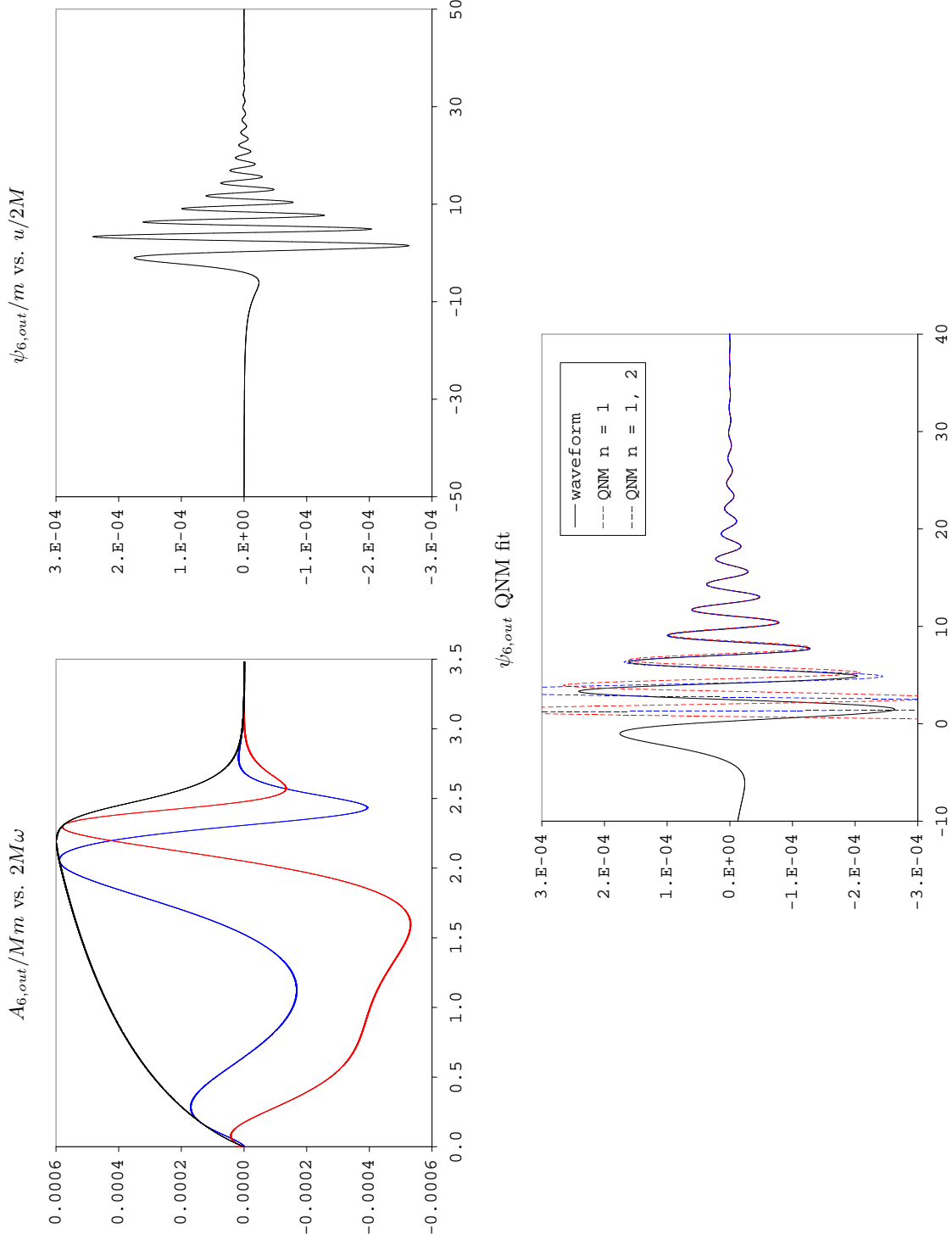FIG. 6: Top left panel: the amplitude $A_{6,out}/Mm$. Top right panel: the waveform $\psi_{6,out}/m$. Bottom panel: the curves corresponding to the QNM contribution up to the second overtone $n = 2$.

$2M\omega_{n,\Im}$ vs. $2M\omega_{n,\Re}$

$B_{l,n}/Mm$ vs. overtone number n

$\theta_{l,n}$ vs. overtone number n

$\omega_{3,1,\Re}$ vs. $[a,b]$

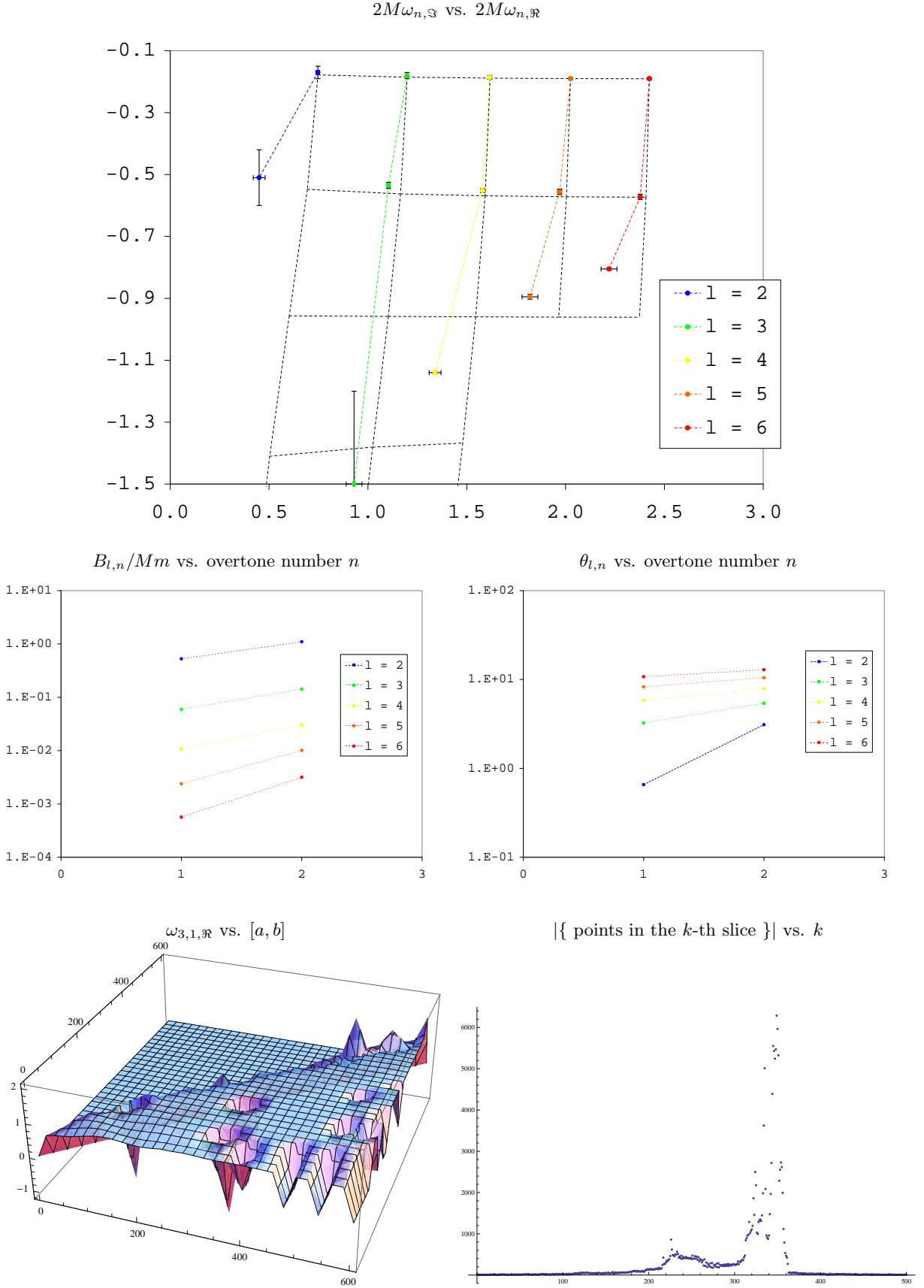$|\{$ points in the k-th slice $\}|$ vs. k

FIG. 7: Top panel: the computed QNMs through the waveforms fit. The dotted lines' intersections are the expected values. Vertical lines link QNMs of the same l while horizontal lines link QNMs with the same n. n increases by going downwards. Middle panels: the amplitudes $B_{l,n}/Mm$ and phases $\theta_{l,n}$ of the first two overtones. Bottom left panel: example of the 3D plot obtained when fitting the waveform for QNMs on all intervals $[a,b]$ in $[0,30]$ of $u/2M$. Bottom right panel: the corresponding histogram giving the number of points in each horizontal slice of the 3D plot.